



HAL
open science

Nano-scale buckling in lamellar block polymers: a molecular dynamics simulation approach

Ali Makke, O. Lame, Michel Perez, Jean-Louis Barrat

► **To cite this version:**

Ali Makke, O. Lame, Michel Perez, Jean-Louis Barrat. Nano-scale buckling in lamellar block polymers: a molecular dynamics simulation approach. 2013. hal-00860951

HAL Id: hal-00860951

<https://hal.science/hal-00860951>

Preprint submitted on 11 Sep 2013

HAL is a multi-disciplinary open access archive for the deposit and dissemination of scientific research documents, whether they are published or not. The documents may come from teaching and research institutions in France or abroad, or from public or private research centers.

L'archive ouverte pluridisciplinaire **HAL**, est destinée au dépôt et à la diffusion de documents scientifiques de niveau recherche, publiés ou non, émanant des établissements d'enseignement et de recherche français ou étrangers, des laboratoires publics ou privés.

Nano-scale buckling in lamellar block polymers: a molecular dynamics simulation approach

Ali Makke,^{*,†,‡,¶} Olivier Lame,^{*,‡} Michel Perez,^{*,‡} and Jean-Louis Barrat^{*,§}

*Université de Lyon- Univ. Lyon I - LPMCN - UMR CNRS 5586- F69622 Villeurbanne, France,
Université de Lyon - INSA Lyon - MATEIS - UMR CNRS 5510 - F69621 Villeurbanne, France,
Ecole Polytechnique Féminine, Institut Charles Delaunay - LASMIS UMR CNRS 6279- F10004
Troyes, France, and Université Joseph Fourier, Grenoble - LIPhy - UMR CNRS 5588- F38402
Grenoble, France*

E-mail: ali.makke@epf.fr; olivier.lame@insa-lyon.fr; michel.perez@insa-lyon.fr;
jean-louis.barrat@ujf-grenoble.fr

Abstract

Oriented block copolymers exhibit a buckling instability when submitted to a tensile test perpendicular to the lamellae direction. In this paper we study this behavior using a coarse grained molecular dynamics simulation approach. Coarse grained models of lamellar copolymers with alternate glassy rubbery layers are generated using the Radical Like Polymerization method, and their mechanical response is studied. For large enough systems, uniaxial tensile tests perpendicular to the direction of the lamellae reveal the occurrence of the buckling instability at low strain. The results that emerge from molecular simulation are compared to an elastic theory of the buckling instability introduced by Read and coworkers. At high strain

*To whom correspondence should be addressed

[†]Université de Lyon- Univ. Lyon I - LPMCN - UMR CNRS 5586- F69622 Villeurbanne, France

[‡]Université de Lyon - INSA Lyon - MATEIS - UMR CNRS 5510 - F69621 Villeurbanne, France

[¶]Ecole Polytechnique Féminine, Institut Charles Delaunay - LASMIS UMR CNRS 6279- F10004 Troyes, France

[§]Université Joseph Fourier, Grenoble - LIPhy - UMR CNRS 5588- F38402 Grenoble, France

rates, significant differences are observed between elastic theory and simulation results for the buckling strain and the buckling wavelength. We explain this difference by the strain rate dependence of the mechanical response. A simple model that takes into account the influence of the strain rate in the mechanical response is presented to rationalize the results at low and moderate strain rates. At very high strain rates, cavitation takes place in the rubbery phase of the sample and limits the validity of the approach.

Introduction

Block copolymers such as (Styrene-Butadiene-Styrene SBS or Styrene-Isoprene-Styrene SIS) have attracted much interest in the past few decades for their use as thermoplastic elastomers. The microstructure of such materials results from the mixture of two different homo-polymers. Interesting combination of properties (similar to the case of nano-composites) at ambient temperature can be obtained when one of the constitutive homo-polymer is hard (glassy or crystalline) while the other one is soft (rubbery). As both constituents are linked together by chemical cross-links, the resulting material combines the mechanical properties of each phase: therefore ductility of the rubbery phase is coupled to the toughness of the glassy phase.

The mechanical response of such composite materials is far from being understood, especially at the molecular scale. Depending on the amount of each component, the thermodynamics equilibrium between phases leads to various morphologies (*e.g.* spherical, cylindrical and lamellar¹). The lamellar morphology is particularly interesting as a model system because the global behavior is not dominated by one of the component. Moreover, the one dimensional aspect of the lamellar morphology is similar to the morphology of semi-crystalline polymers at small scale.

Such nano-structured materials exhibit similar mechanical behavior ²⁻⁵ through complex deformation mechanisms when they are stretched perpendicular to the lamellae direction: the hard lamellae buckle, forming a “chevron-like” morphology. This phenomenon has been observed in semi-crystalline polymers by several authors ^{6,7} and more recently by Bartczak and Mohanraj ^{8,9}. Buckling of hard lamellae is of prior importance regarding the mechanical properties of nanostruc-

tured polymers: it induces a rapid collapse of the hard phase network which can be an initiator of the macroscopic yield, decreasing thus the mechanical properties of the material.

Several experimental works^{10–15} were focused on the formation of “chevron” in block-copolymers using *in situ* Small Angle X-ray Scattering (SAXS). The results reveal a progressive modification of the SAXS pattern at yield, from two spots to four symmetric spots, which is the signature of the “chevron” morphology (see 1).

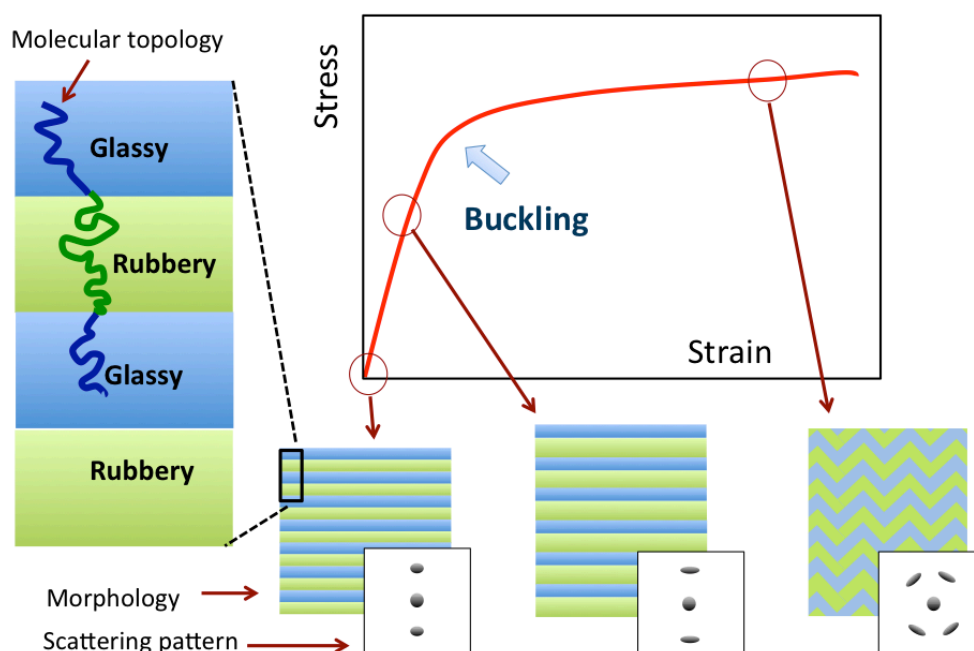


Figure 1: Schematic description: Evolution of a triblock morphology from lamellar to chevron-like morphology under tensile test conditions. This transformation separates two regimes: (i) the elastic regime, (ii) the buckling regime. A schematic description of the phases topology is shown at left. The corresponding SAXS pattern are shown in the inset.

Buckling was also observed by a direct examination of the microstructure of highly deformed SBS samples using atomic force or electron microscopy.^{16,17} The origin of buckling is interpreted from the contrast in the elastic properties of the glassy and rubbery layers. As the rubbery layer accommodates most of the imposed deformation, it tends to contract in the transverse direction. The strong coupling between phases leads to a compressive stress in the transverse direction of the glassy layer. As a consequence, the glassy lamellae buckle to form a “chevron” morphology.

These qualitative explanations are well established. However, the attempts to model the phe-

nomenon theoretically are scarce, and essentially at the level of a continuum description. In a pioneering work, Read *et al*¹⁸ proposed an original energetic approach to describe the competition between buckling and affine deformation, and proved with Finite Element Methods (FEM) that this instability can occur even in the pure elastic regime. Unfortunately, this purely elastic approach ignores visco-elastic or rate dependent effects, and does not account for the competition with other failure modes such as cavity nucleation.

In this paper, we study the initiation of the buckling instability and the mechanical response of a block copolymer model using coarse grained molecular dynamics simulations. This numerical tool is indeed particularly adapted to study this problem as it intrinsically contains elasticity, viscosity, and all associated dynamical effects. It also accounts for defects, and for the different coupling strengths that can exist between phases, depending on the density of tie molecules.¹⁹ Moreover, coarse grained MD permits the study of buckling well above the yield stress in the plastic regime, where other instabilities such as cavitation can occur.²⁰ The approach gives access to the local measurement of many variables (*e.g* local stress, local density) while monitoring the global mechanical behavior. This allows one to investigate the relationship between the mechanical response and the change in the local microstructure and morphology.

This paper is a companion paper of a previously published report,²¹ which showed the feasibility of such an approach and gave a preliminary account of the results. Section II presents the model and the methods that are used in this study. Section III discusses the relationship between the microstructure and the associated stress-strain curve. Section IV recalls the formalism introduced by Read *et al*.¹⁸ The following sections detail the effect of sample size (section V) and strain rate (section VI). A simple kinetic model predicting the competition between buckling modes is finally presented in section VII and compared with MD results.

Method and model

The molecular dynamics model

Molecular dynamics (MD) simulations were carried out for a well established coarse-grained model,²² in which the polymer is treated as a chain of N beads, which we refer to as monomers, of mass $m = 1$ connected by a spring to form a linear chain. The beads interact with a classical Lennard-Jones (LJ) interaction :

$$U_{\text{LJ}}^{\alpha\beta}(r) = \begin{cases} 4\varepsilon_{\alpha\beta} \left[\left(\frac{\sigma_{\alpha\beta}}{r} \right)^{12} - \left(\frac{\sigma_{\alpha\beta}}{r} \right)^6 \right] & , r \leq r_c \\ 0 & , r > r_c \end{cases} \quad (1)$$

where the cutoff distance $r_c = 2.5\sigma$. α and β represent the chemical species (*i.e.* A, B) In addition to (1), adjacent monomers along the chains are coupled through the well known anharmonic Finite Extensible Nonlinear Elastic potential (FENE):

$$U_{\text{FENE}}(r) = -0.5kR_0^2 \ln \left[1 - \left(\frac{r}{R_0} \right)^2 \right], r \leq R_0 \quad (2)$$

The parameters are identical to those given in Kremer *et al.*,²² namely $k = 30\varepsilon/\sigma^2$ and $R_0 = 1.5\sigma$, chosen so that unphysical bond crossings and chain breaking are avoided. All quantities will be expressed in terms of length σ , energy ε , pressure ε/σ^3 and time $\tau = \sqrt{m\sigma^2/\varepsilon}$.

Newton's equations of motion are integrated with the velocity Verlet method and a time step $\Delta t = 0.006\tau$. Periodic simulation cells containing $340 \times n$ chains (n is the replication number - see below) of $N = 200$ beads were used with a Nosé-Hoover barostat, *i.e.* in the NPT ensemble. An anisotropic barostat with $P_x = P_y = P_z = 0$ is used in the equilibration, leading to a tetragonal simulation box before running the tensile test.

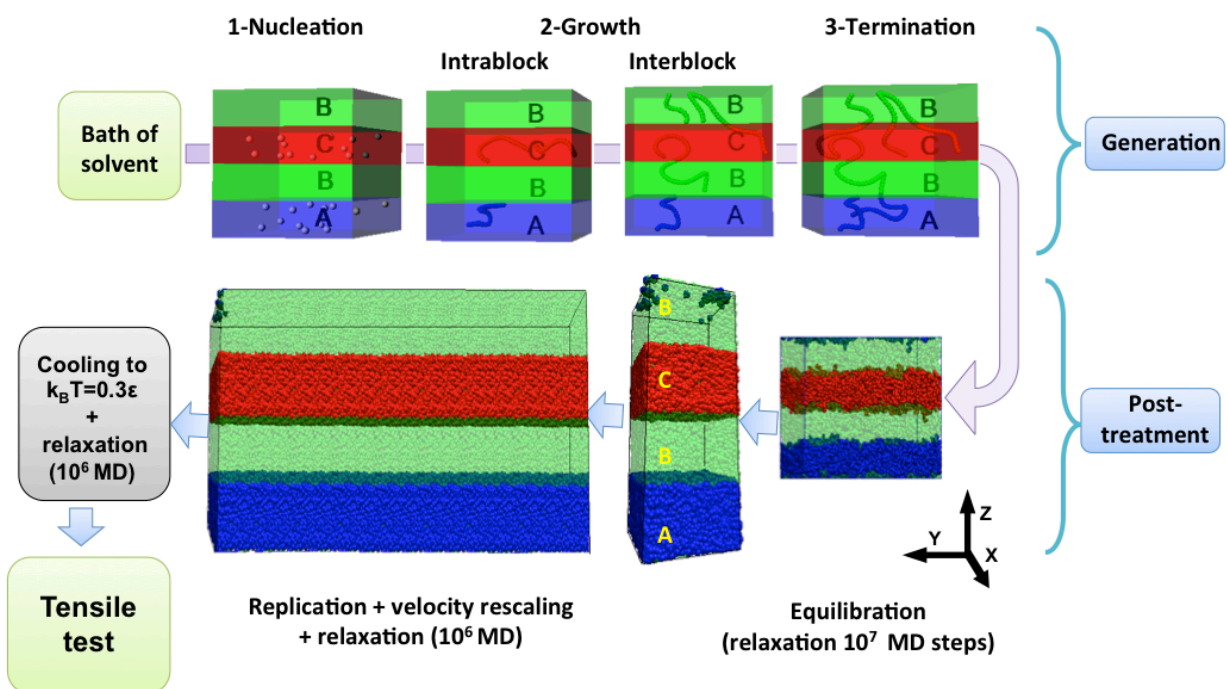


Figure 2: Schematic description of the generation and the post treatment process. Starting from a bath of monomers ("solvent"), the Radical Like Polymerization routine will transform the single disconnected beads to entangled chains. The polymerization occurs in 4 blocs A, B, C and B. The resulting chains are shared between three successive blocks A, B and C. LJ interaction energies are chosen so that a perfect segregation of the blocks is ensured at low temperature.

Polymer sample generation

Our samples have been generated using the “Radical-Like Polymerization” (RLP) method.²³ The polymerization takes place in a LJ liquid bath (solvent) for which $\epsilon_{\alpha\beta} = 1 \epsilon$ and $\sigma_{\alpha\beta} = 1 \sigma$ for all LJ interactions. A set of 340 monomers are chosen as “radicals”. The growth of chains is then performed by a sequence of bead-addition (growth) and subsequent relaxation. In the growth stage, each radical captures one of its free nearest neighbors and a covalent bond is created between them. The newly bonded monomer becomes itself a radical. After that, the system is relaxed during 500 MD steps at $k_B T = 1 \epsilon$. Then, a new growth step is performed, until chains reach the desired size.

This concept was adapted to generate triblock copolymer samples with four distinct blocks $ABCB$ and four interfaces parallel to the (xy) plane. The generation starts simultaneously in blocks A and C . When the chains reach a length of $N/4$, the radical is dragged towards the nearest interface to complete the growth of chain in neighboring blocks B . After the chain reaches a length of $3N/4$, the radical, that started growth in block A moves to achieve the polymerization in block C and *vice-versa*. The generation is stopped when all chains attain the request length N . The generation method is detailed in references.^{19,23}

Equilibration and replication

After the sample has been generated, the remaining solvent is removed from the simulation box. The LJ interaction energies are then adjusted to drive the segregation and associated block thickness. In this study, the LJ energies are chosen such that A and C layers are glassy, while B layer is rubbery: $\epsilon_{AA} = \epsilon_{CC} = 1 \epsilon$, $\epsilon_{BB} = 0.3 \epsilon$ and $\epsilon_{AB} = \epsilon_{BC} = 0.4 \epsilon$. The system is then relaxed 10^7 MD steps in NPT ensemble at $k_B T = 1 \epsilon$. All the pressure components are maintained at zero ($P_x = P_y = P_z = 0$) using an anisotropic barostat, allowing box changes in the three dimensions independently. The evolution of the box lengths during the relaxation steps has been measured and it has been found that the box dimensions reach a steady state after 10^7 MD steps, indicating that mechanical equilibrium is reached.

In order to study the effect of sample size, larger samples were built by replicating several times

the basic periodic sample in the y direction. The replication was performed at $k_B T = 1\epsilon$ where the two phases are rubbery. To avoid unphysical internal periodicity, bead velocities are rescaled and an additional 10^6 MD steps are performed. After this relaxation stage, each sample is cooled down to a temperature of $k_B T = 0.3\epsilon$ during 7×10^5 MD steps and relaxed again 10^6 MD steps. Four different box sizes (in the y direction) have been investigated: 200, 400, 500 and 800σ .

Finally, the glass transition temperatures of each phase were determined from volume curves at constant pressure, and it was found that $T_g^A = 0.43$ and $T_g^B = 0.20$. In the following the system will be studied at a temperature intermediate between T_g^A and T_g^B , so that the B phase has the properties of a rubber and the A phase those of a glass. 2 describes schematically the sequence operations for both generation and post treatment stages of the sample.

Tensile test:

To deform our samples, uniaxial homogenous tensile test conditions were employed.²⁰ The samples were subjected to a sequence of deformation-relaxation steps, composed of: (i) a rescaling of the simulation box in the tensile direction (Z in our case, so that the true strain is $\epsilon_{zz}(t) = \ln(L_z(t)/L_z(0))$); and, (ii) one MD step in the NPT ensemble at $k_B T = 0.3 \epsilon$ and $P_x = P_y = 0$ (Nosé-Hover anisotropic barostat is employed to control the pressure only in x and y directions independently). The tensile velocity \dot{L}_z was chosen so that the initial strain rate is $\dot{\epsilon}_{yy}(0) = 7.3 \times 10^{-5} \tau^{-1}$ (high strain rate tests) and $\dot{\epsilon}_{yy}(0) = 1.4 \times 10^{-5} \tau^{-1}$ (low strain rate tests).

stress/strain curve

In order to study the correlation between the mechanical response and the change of the sample morphology, we start by presenting the results of uniaxial tensile test on “large” ($L_Y \simeq 400\sigma$) samples. The tensile strain was applied in the Z direction (perpendicular to the lamellae) at a constant velocity $V_z = \dot{L}_z$. In this first set of results, the strain rate is $\dot{\epsilon}_{zz} = 7.3 \times 10^{-5} \tau^{-1}$ and the initial size of the simulation box is $(32.4 \times 74.2 \times 393.6) \sigma^3$. The resulting stress-strain curve is

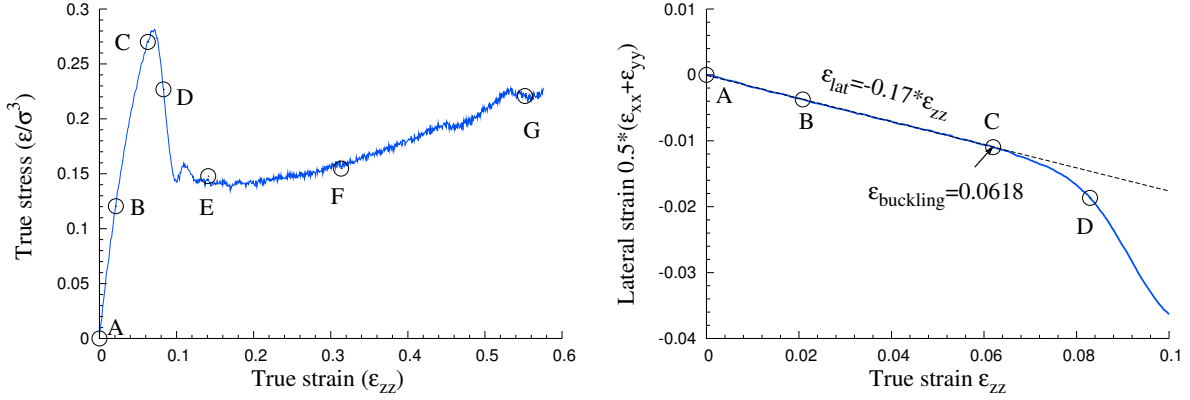


Figure 3: Left-panel: Stress strain curve of a sample submitted to a uniaxial tensile test in the direction normal to the layers (Z direction). The black circles correspond to the density maps shown in figure 4. Right panel: Lateral strain in the same sample with respect to the tensile strain. The first linear part of the curve fits the Poisson ratio of the sample in the elastic regime. The curve deviates from this linear behavior after buckling has occurred.

plotted in figure 3. During the tensile test, sample configurations were stored at different strains. Figure 4 shows the local density map of such configurations, where the glassy and the rubbery phases can be distinguished by the high and low density lamellae, respectively.

The stress-strain curve in figure 3 exhibits different regimes. In the first elastic regime the stress growth linearly. This response results from the serial coupling of the lamellae and the imposed strain is mainly accommodated by the deformation of the soft phase (rubbery). Beyond the elastic regime a progressive softening is observed. This softening is correlated to a progressive change in the morphology of the sample, as the aligned lamellae start to buckle, leading to an undulated pattern. Buckling is signaled by a drastic change of the apparent Poisson ratio, illustrated in Figure 3-right, which displays the lateral strain as a function of the imposed normal strain. The first linear part of the curve corresponds to the linear elastic regime, and the slope gives the apparent Poisson ratio of the sample. A sudden decrease of the Poisson ratio appears when the buckling starts. After the onset of buckling, cavities nucleate in the rubbery phase, leading thus to a strong drop in the stress. Figure 4 shows the nucleation and the evolution of the cavities (low density spots in the rubbery phase). With increasing strain the amplitude of the buckling undulation develops. The cavities that are first randomly nucleated in the rubbery phase, become progressively localized at

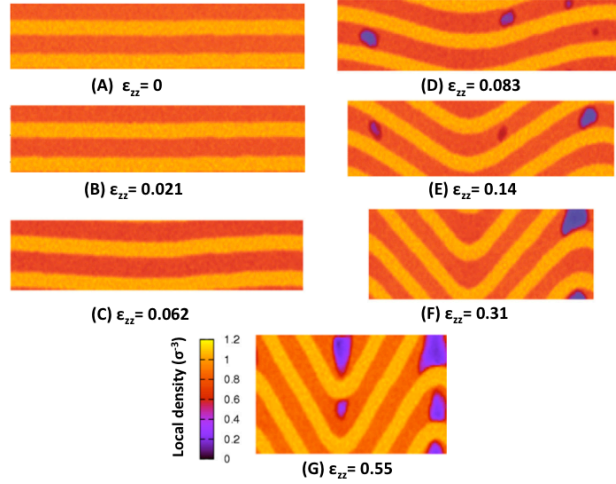


Figure 4: Local density cartography of the tested sample at several strains. The color contrast illustrates the alternance of glassy and rubbery lamellae with high and low density, respectively. As the deformation progresses, nucleation of cavities occurs randomly in the rubbery phase. Cavities that are located in the tilted part of the chevron disappear, as the deformation in these regions becomes a simple shear deformation; however, only cavities that are located in the hinges, where the deformation is effectively triaxial, persist to a high strain.

the hinges of the pattern. Indeed, cavities nucleated in the tilted part of the buckle tend to heal, as the stress in these regions becomes a simple shear. On the contrary, the stress at the hinges is essentially triaxial, and favors cavitation.

The micro-mechanical origin of buckling instability has been elucidated in reference.²¹ Due to the serial coupling between the glassy and rubbery phases, the tensile strain will be mainly localized in the rubbery lamellae. The tensile strain in the normal direction of the layers will be converted locally to a contraction in the transverse direction because of the Poisson effect in the rubber. This lateral contraction will be transmitted to the glassy phase via the interface, then a compressive stress acts on the transverse direction of the glassy lamellae. Under these conditions, and for a sufficiently large system, a buckling instability takes place to relax the lateral compressive stress.

Theoretical modeling of buckling instability

The development of a buckling instability in a layered material with alternative hard and soft blocks can be studied using elasticity theory. The volume average elastic energy density of a homogeneously strained sample is, as usual, given by:

$$\langle e \rangle = \frac{1}{2} C_{ijkl} \langle \varepsilon_{ij} \varepsilon_{kl} \rangle \quad (3)$$

where ε_{ij} are the components of the macroscopic strain, and C_{ijkl} the elastic constants. For the sake of simplicity, only a 2D case is presented here: the x direction is parallel to the lamellae, and z the direction of traction, perpendicular tot the lamellae. Taking into account the symmetry of our system (transversely isotropic - see 2), the volume averaged elastic energy density reduces to:

$$2\langle e \rangle = C_{11} \langle \varepsilon_{11}^2 \rangle + C_{33} \langle \varepsilon_{33}^2 \rangle + 2C_{13} \langle \varepsilon_{33} \varepsilon_{11} \rangle + 2C_{44} \langle \varepsilon_{13}^2 \rangle \quad (4)$$

where standard Voigt notations have been used. Here the energy density is expressed in a local frame that is aligned with the lamellar pattern, as will become clear below. The elastic constants are the effective values that describe the lamellar material as a whole, and depend from the characteristics of each phase. A particularity of the dibloc material resides in the values of these elastic constants (see table 1). The material is remarkably soft when submitted to shear in the xz or yz directions. Therefore, when submitted to a tensile stress in the z direction, the material will have a tendency to locally *rotate* in order to align its soft directions at 45° from the direction of traction.

Table 1: Elastic constants of the layered bock copolymer studied in this paper. Elastic constants have been determined with molecular statics on a stress-free sample by applying small perturbation in the box shape. For the sake of comparison, the Young modulus of a glassy polymer is of order $50 \varepsilon/\sigma^3$

	C_{11}	C_{33}	$C_{23} = C_{13}$	$C_{44} = G$	ν
$[\varepsilon/\sigma^3]$	24	7.6	6.5	0.07	0.18

The formalism of equation 4, which assumes a homogeneous strain, is not appropriate to predict such a rotation, and in principle a full finite element calculation involving space varying elastic constants appropriate for the different phases would be required. The analysis proposed by Read *et al*¹⁸ bypasses this difficulty, by describing the local deformation of the sample ϵ_{ij} as a combination of a “shear+strain” deformation expressed in the local frame of the lamellae (through ϵ_{11} , ϵ_{13} and ϵ_{33} - transformation matrix $[\mathcal{S}]$) with a space dependent rotation θ (transformation matrix $[\mathcal{R}]$), which describes the local tilt of the lamellar structure. The two transformation matrixes that describe these deformations are:

$$[\mathcal{R}] = \begin{bmatrix} \cos \theta & -\sin \theta \\ \sin \theta & \cos \theta \end{bmatrix} \text{ and } [\mathcal{S}] = \begin{bmatrix} 1 + \epsilon_{11} & \epsilon_{13} \\ 0 & 1 + \epsilon_{33} \end{bmatrix} \quad (5)$$

Under deformation, two adjacent points $M_0(x_0, z_0)$ and $M(x_0 + \delta x, z_0 + \delta z)$ are transformed into $M'_0(x'_0, z'_0)$ and $M'(x'_0 + \delta x', z'_0 + \delta z')$, and the vector $\mathbf{M}\mathbf{M}_0$ experiences the combination of the rotation and deformation:

$$\mathbf{M}'\mathbf{M}'_0 = [\mathcal{R}][\mathcal{S}]\mathbf{M}\mathbf{M}_0 \quad (6)$$

In terms of the coordinates, this reads:

$$\begin{pmatrix} \delta x' \\ \delta z' \end{pmatrix} = \begin{bmatrix} \cos \theta & -\sin \theta \\ \sin \theta & \cos \theta \end{bmatrix} \begin{bmatrix} 1 + \epsilon_{11} & \epsilon_{13} \\ 0 & 1 + \epsilon_{33} \end{bmatrix} \begin{pmatrix} \delta x \\ \delta z \end{pmatrix} \quad (7)$$

If one now introduces the displacement field $\mathbf{v}(x, z)$ such that $\mathbf{M}'_0 = \mathbf{M}_0 + \mathbf{v}(x_0, z_0)$, the relation between $\mathbf{M}'\mathbf{M}'_0$ and $\mathbf{M}\mathbf{M}_0$ is expressed in terms of the displacement gradients:

$$\begin{pmatrix} \delta x' \\ \delta z' \end{pmatrix} = \begin{pmatrix} \delta x \\ \delta z \end{pmatrix} + \begin{bmatrix} \nabla_x v_x & \nabla_z v_x \\ \nabla_x v_z & \nabla_z v_z \end{bmatrix} \begin{pmatrix} \delta x \\ \delta z \end{pmatrix} \quad (8)$$

Combining equations 7 and 8 leads to a system of 4 equations that can be inverted to give θ , ϵ_{11} , ϵ_{13} and ϵ_{33} in terms of the displacement gradient $\nabla \mathbf{v}$:

$$\begin{cases} \sin \theta = \nabla_x v_z / \Delta \\ \epsilon_{11} = \Delta - 1 \\ \epsilon_{33} = [(1 + \nabla_z v_z)(1 + \nabla_x v_x) - \nabla_z v_x \nabla_x v_z] / \Delta - 1 \\ \epsilon_{13} = [(\nabla_z v_x)(1 + \nabla_x v_x) + (\nabla_x v_z)(1 + \nabla_z v_z)] / \Delta \end{cases} \quad (9)$$

where $\Delta = \sqrt{(\nabla_x v_z)^2 + (1 + \nabla_x v_x)^2}$. Note that if the sample is submitted to pure shear, such as only $\nabla_x v_z \neq 0$, $\sin \theta = \epsilon_{13}$, *i.e.* the shear is completely described by the local rotation.

In order to describe an undulating pattern of the lamellar structure, the global displacement vector \mathbf{v} is decomposed in two contributions: the macroscopic deformation of the sample (strains ϵ_{xx} , ϵ_{xz} and ϵ_{zz}) and a small perturbation that imposes a displacement along z only: $\mathbf{u} = u_z(x)\mathbf{z}$:

$$\begin{cases} v_x = \epsilon_{xx}x \\ v_z = \epsilon_{zz}z + u_z \end{cases} \quad (10)$$

where $u_z(x) = U_0 \sin(kx)$ is a sinusoidal small perturbation of wave vector k that describes the local displacement due to buckling.

Now, it is possible to calculate local deformations ϵ_{11} , ϵ_{13} and ϵ_{33} of equation 11 using the decomposition described in equation 10. Only second order terms of the small sinusoidal perturbation U_0 are retained, leading to the following expressions for the local deformations in the frame of the lamellae:

$$\begin{cases} \langle \epsilon_{11}^2 \rangle = \epsilon_{xx}^2 + \frac{U_0^2 k^2}{2(1+\epsilon_{xx})^2} \epsilon_{xx} (1 + \epsilon_{xx}) \\ \langle \epsilon_{33}^2 \rangle = \epsilon_{zz}^2 - \frac{U_0^2 k^2}{2(1+\epsilon_{xx})^2} \epsilon_{zz} (1 + \epsilon_{zz}) \\ \langle \epsilon_{11} \epsilon_{33} \rangle = \epsilon_{xx} \epsilon_{zz} + \frac{U_0^2 k^2}{4(1+\epsilon_{xx})^2} (\epsilon_{zz} - \epsilon_{xx}) \\ \langle \epsilon_{13}^2 \rangle = \frac{U_0^2 k^2}{2(1+\epsilon_{xx})^2} (1 + \epsilon_{zz})^2 \end{cases} \quad (11)$$

It is worth noting that, for a tensile test along the z axis ($\epsilon_{xx} < 0$ and $\epsilon_{zz} > 0$), the rotation introduced previously induces a net decrease in the squared local deformations, leading to an energy relaxation and demonstrating thus the possibility for an instability.

Inserting the identities above into the energy density equation 4 leads to the volume averaged

elastic energy density:

$$2\langle e \rangle = C_{11}\epsilon_{xx}^2 + 2C_{13}\epsilon_{xx}\epsilon_{zz} + C_{33}\epsilon_{zz}^2 + \frac{1}{2}U_0^2k^2f_1^{2D} \quad (12)$$

where

$$f^{2D} = [G - \epsilon_{zz}(C_{33} - C_{13} - 2G) - \epsilon_{zz}^2(C_{33} - G) + \epsilon_{xx}(C_{11}(1 + \epsilon_{xx}) - C_{13})]/(1 + \epsilon_{xx})^2 \quad (13)$$

Due to the specific moduli of our composite system (see table 1), the term f^{2D} , slightly positive at zero strain, rapidly turns negative as strain increases (*i. e.* after less than 1% deformation in z). Thanks to this combination of transformations, the local shear in the xz plane is completely handled by the rotation θ , decreasing the elastic energy of the system and causing thus the buckling instability.

However, in equation 12, there is no cost associated with the sinusoidal bending of the material, except the shearing of the soft phase, which is, as mentioned previously, very low. In order to account for the energy associated with the bending of the composite, and particularly the bending of the hard phase, a new term has to be added. It is assumed here, following the idea of Read *et al*, that only the hard layers contribute to the bending energy. A macroscopic expression is then introduced from beam mechanics, which gives the energy, that is necessary to bend a plate:

$$e_b = \frac{1}{2}K(\nabla_x\theta)^2 \quad (14)$$

where K is the bending modulus of the sample. Due to the serial coupling between phases the bending modulus will be dominated by the contribution of the hard phase. The bending modulus can then be estimated from simple beam bending theory as $K = \phi_h^3 E_h d^2 / [12(1 - \nu_h^2)]$ where ϕ_h is the volume fraction of the hard phase, E_h and ν_h are the Young's modulus and Poisson ratio of the hard phase and d is the lamellar spacing.

The total energy density results from the addition of the bulk elastic energy and the bending

energy, $\langle e_T \rangle = \langle e_b \rangle + \langle e \rangle$:

$$2\langle e_T \rangle = C_{11}\epsilon_{xx}^2 + 2C_{13}\epsilon_{xx}\epsilon_{zz} + C_{33}\epsilon_{zz}^2 + F(\epsilon_{zz}, k) \quad (15)$$

with $F(\epsilon_{zz}, \epsilon_{xx}, k) = (U_0^2/2)(k^2 f^{2D} + Kk^4)$. In the real 3D case, the same analysis can be performed, which leads to a function f^{3D} instead of f^{2D} where:

$$f^{3D} = f^{2D} - \frac{C_{23}\epsilon_{yy}}{(1 + \epsilon_{xx})^2} \quad (16)$$

This leads to the final form of the function $F(\epsilon_{xx}, \epsilon_{yy}, \epsilon_{zz}, k)$:

$$F(\epsilon_{xx}, \epsilon_{yy}, \epsilon_{zz}, k) = \frac{U_0^2}{2}(k^2 f^{3D} + Kk^4) \quad (17)$$

The buckling instability occurs upon increasing strain when the function $F(\epsilon_{xx}, \epsilon_{yy}, \epsilon_{zz}, k)$ in equation 15 becomes negative, meaning that the global gain in elastic energy overwhelms the bending energy penalty.

Finally, before the buckling begins (*i.e.* in the elastic regime) ϵ_{xx} and ϵ_{yy} can be replaced by $\nu\epsilon_{zz}$ where ν is a global Poisson ratio. Under this assumption, $f^{3D}(\epsilon_{xx}, \epsilon_{yy}, \epsilon_{zz})$ becomes $f^{3D}(\epsilon_{zz})$ and $F(\epsilon_{xx}, \epsilon_{yy}, \epsilon_{zz}, k)$ becomes $F(\epsilon_{zz}, k)$.

Figure 5 shows the evolution of $F(\epsilon_{zz}, k)$ as a function of the wave-vector k for several tensile strains ϵ_{zz} . At low strain $F(\epsilon_{zz}, k_n)$ is positive for any possible wave-vector k , therefore the buckling is impossible. As the tensile strain increases $F(\epsilon_{zz}, k_n)$ becomes negative for a wave-vector range, which indicates the possibility of buckling.

Note that the periodic boundary conditions imposed in the direction y in our MD simulations limit the possible wavevectors to the discrete set:

$$k = k_n = n \frac{2\pi}{L_y} \quad (18)$$

where n is the mode number; *i.e.* $n = 1$ is the fundamental mode where the wavelength of the

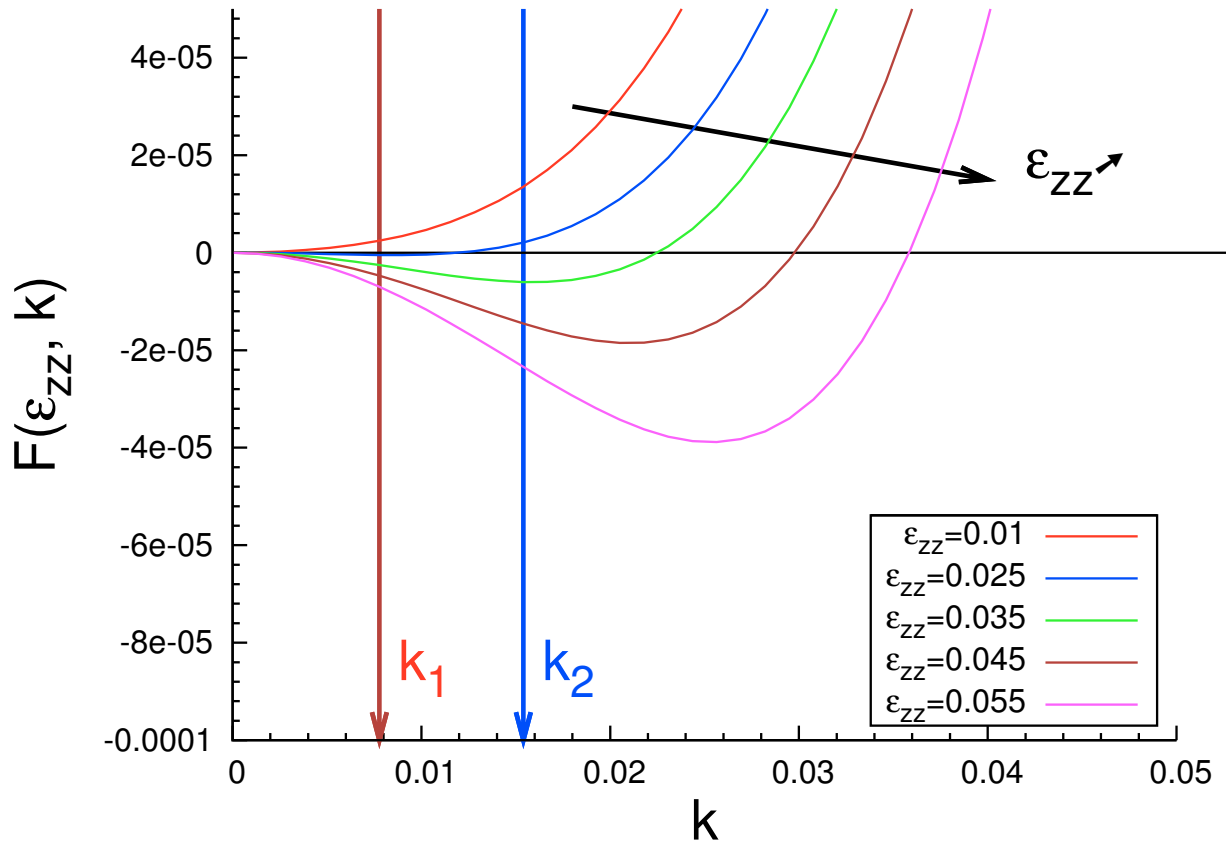


Figure 5: Evolution of $F(\varepsilon_{zz}, k)$ (see equations 15 and 17) for different levels of strain, the two arrows denote the wavevectors $k_1 = 2\pi/L_y$ and $k_2 = 4\pi/L_y$.

perturbation is equal to the sample size. Figure 5 shows that as deformation increases, the first wavelength for which the sinusoidal perturbation might be stable is the fundamental one. As the deformation increases, the fundamental mode might not be the most energetically favorable, since larger wave-vectors lead to more negative values for $F(\epsilon_{zz}, k_n)$.

Finally, buckling occurs if:

$$f^{3D}(\epsilon_{zz}) + K \left(n \frac{2\pi}{L_y} \right)^2 < 0 \quad (19)$$

Resolution of equation 19 leads to a prediction of the strain at which buckling should appear as a function of sample length L_y for a given mode n (see 10).

In the next section, we present a comparison between our MD simulations and this linear stability analysis.

Influence of the sample size

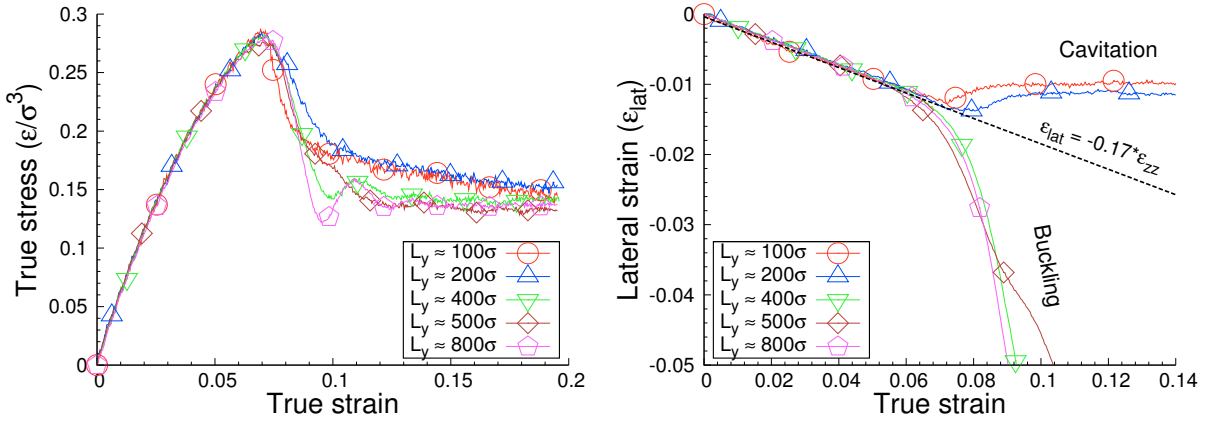


Figure 6: Left panel: Comparison between the mechanical responses of several samples with different sizes, the strain rate is $\dot{\epsilon}_{zz} = 7.3 \times 10^{-5}$ for all samples. The corresponding lateral strain curves are shown in the right-panel. All curves have the same yield point; however, the largest three samples exhibit buckling while only cavitation is present in the two smaller samples. (see the snapshots in figure 9). When buckling is observed, the buckling strain is roughly independent of sample size, which is in contrast with the prediction from elastic theory.

According to the elastic theory, the instability will take place at smaller strains for bigger sam-

ples, and always at the largest possible wavelength allowed by the boundary conditions. We have therefore studied several samples with different sizes. These samples were created by replicating the *same* elementary cell i times along the Y direction, where $i = 3, 6, 12, 15$ and 24 times. Because of the periodic boundary conditions, the buckling wave length must be an integer subdivision of the sample size, $k_n = n \times \frac{2\pi}{L_y}$.

Figure 6 compares the mechanical response of all tested samples, at the same strain rate $\dot{\epsilon}_{zz} = 7.3 \times 10^{-5}$. In terms of stress-strain relation (figure 6.a), all samples have roughly the same mechanical response up to the yield point. The drawing regimes exhibits important differences between smaller and larger samples. The stress softening in large samples is more pronounced than in the small ones. Indeed, both cavitation and buckling can limit the stress growth of the elastic regime, leading then to a stress drop. For long samples, the two mechanisms participate in the stress softening, thus the drop of stress will be increased compared to the short sample case where only cavitation is present.

The right panel in figure 6 shows the lateral strain in the different samples. All curves fit very well the same Poisson ratio in the first linear part (dashed line). After the yield strain, strong deviations can be observed: the lateral strain decreases for long samples ($L_y \geq 393.6\sigma$) while it increases for the shorter ones ($L_y \leq 196.8\sigma$). The decrease in lateral strain is related to buckling instability, as described previously. For short samples, the increase of lateral strain after the yield is correlated with the nucleation of cavities in the rubbery phase. The buckling in such samples is completely absent, as shown in the snapshots of figure 9.

Examining the behavior of the different samples, one concludes that the minimal length for observing buckling before cavitation is between $196.8 \leq L_y^* \leq 393.6$. For samples larger than 393.6σ , the onset of buckling occurs always at the same strain ($\epsilon_{buck} = 0.06$), in contradiction with the expectation from the elastic description of the previous section. A tentative explanation of this behavior will be given below, when we study the influence of the strain rate. Another surprising observation, illustrated in figure 9, is that the wavelength of the instability does not appear to increase with the size of the system, again in contradiction with the expectation from

elastic theory.

Mechanical behavior at lower strain rate

The observations from the section show a difference between the predicted buckling strain and the measures made by simulation. In order to interpret this difference, we inspect in this section the influence of the strain rate on the mechanical response. The same samples described in the previous section will now be submitted to a similar tensile test, at a strain rate that is smaller by a factor of approximately 5.

Stress-Strain response

7 shows the results of a tensile test performed under the same conditions as in section , except for the strain rate which is 5 times smaller, $\dot{\epsilon}_{yy} = 1.4 \times 10^{-5}$. The resulting stress-strain curve, superimposed with the evolution of lateral strain, are shown in the top panel. The linear part of both curves corresponds to the elastic regime (the stress strain curve fits the Young modulus in this regime and the lateral strain curve fits the Poisson ratio). The end of this regime is marked by the yield, followed by a stress softening in stress-strain curve. The yield point corresponds to the onset of buckling, also indicated by the change of the apparent Poisson ratio in the lateral strain curve. The absence of cavities was checked by inspecting the local density of the sample at different strain levels. Therefore, the yield and the stress softening in this case is correlated only to the onset and the development of the buckling in the sample. The last part of the stress-strain curve is the drawing regime, that corresponds to the development of the buckling undulation in an “accordion” like manner. Note that the range of strain studied here is relatively small, so that the strain hardening regime is not attained.

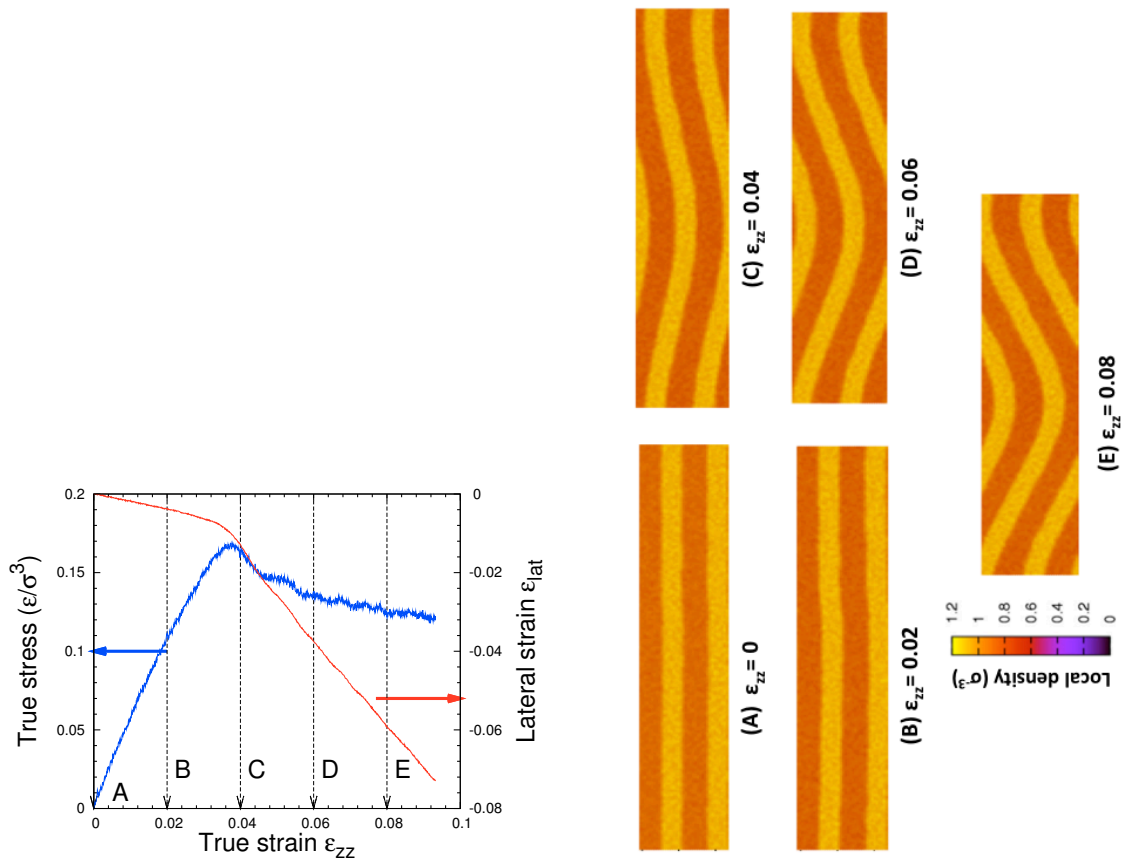


Figure 7: Low strain rate tensile test: the upper panel shows the stress strain curve for the same sample illustrated in figure 3, together with the evolution of the lateral strain. In this case, the yield corresponds to the onset of the buckling. The arrows indicate the strain levels at which the snapshots presented in the lower panel are taken. Cavities are completely absent from the rubbery phase.

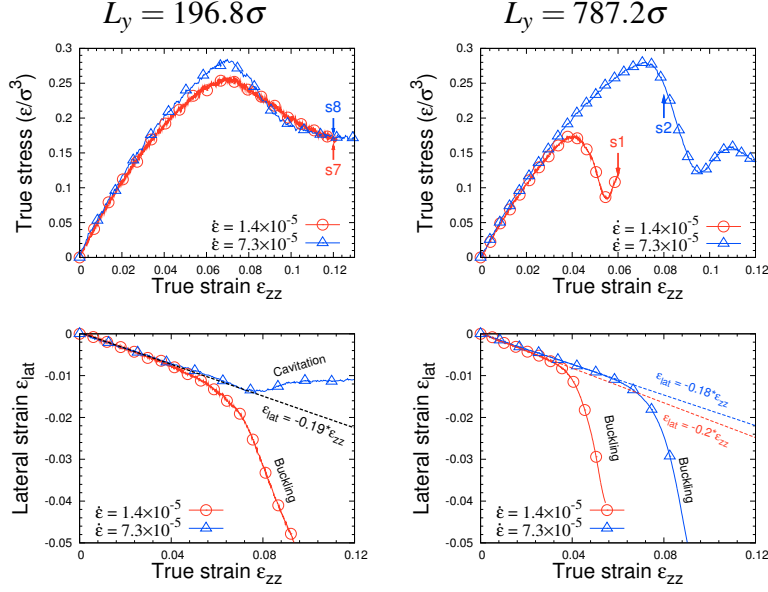


Figure 8: Upper panel: stress-strain curves of the largest and the shortest samples compared at two different strain rates $\dot{\epsilon}_{zz} = 7.3 \times 10^{-5}$ and $\dot{\epsilon}_{zz} = 1.4 \times 10^{-5}$, the lateral strain curves are shown in the lower panel. For the largest sample, decreasing the strain rate will decrease the yield and the buckling strain. This behavior is correlated to the change of the buckling mode as illustrated in figure 9. For the shortest sample, the behavior changes from cavitation to buckling (see figure 9).

Influence of sample size and of strain rate

In figure 8, we compare the stress-strain and the lateral strain curves of our smaller and larger samples, for the two strain rates under consideration. Clearly the Young modulus is essentially independent of system size and strain rate. In contrast, the yield stress and strain decrease as the strain rate decreases, most markedly in the larger sample. Finally, the stress softening is significantly weaker at low strain rate, again especially in the large sample.

In general, the decrease of the yield threshold is strongly correlated with the change of the plastic deformation mode from cavitation to buckling¹. Both cavitation and buckling result in a yield behavior, however the yielding associated with buckling is much more progressive and smooth than the one associated with cavitation. For the smallest sample ($L_y = 196.8\sigma$), the lateral strain curve also highlights a radical change of the mechanical response from cavitation to buckling at low strain rate.

¹The occurrence of buckling for all samples at low strain rate is illustrated in figure 9

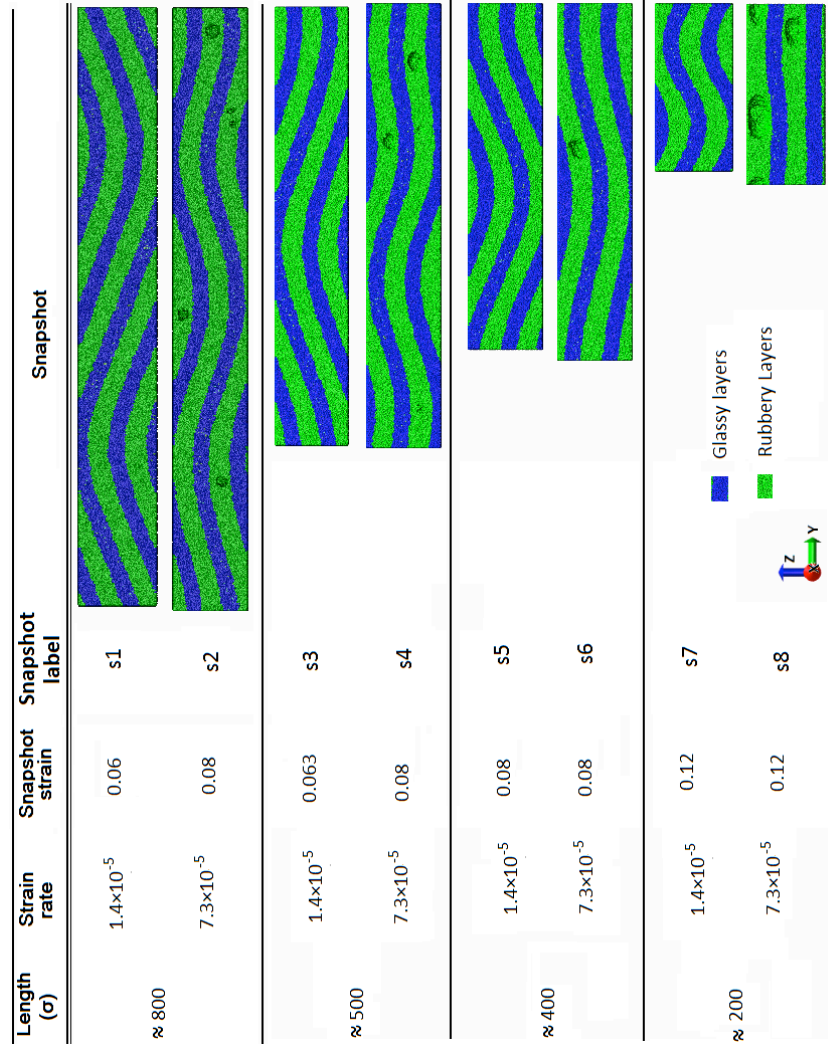


Figure 9: Snapshots show several samples under a uniaxial tensile tests driven by two different strain rates $\dot{\epsilon}_{zz} = 7.3 \times 10^{-5}$ and $\dot{\epsilon}_{zz} = 1.4 \times 10^{-5}$. Several lengths are presented, at low strain rate all samples buckle. The buckling wave length is equal to the sample length. At high strain rate, the buckling wave length seems to be independent from the sample length. The labels correspond to those indicated in figure 8

Figure 9 compares the configurations after buckling, at two different strain rates. The change of the yield mechanism from cavitation to buckling is well illustrated in these snapshots especially for the smallest sample. The second important observation is that the wavelength becomes equal to the sample length in all samples at low strain rate. Finally, there are no cavities present in the rubbery phase of the lower strain rate configurations, compared to systems deformed at high strain rate for the same strain. These snapshots confirm that the low energy buckling mode is adopted by the sample at the lowest strain rate.

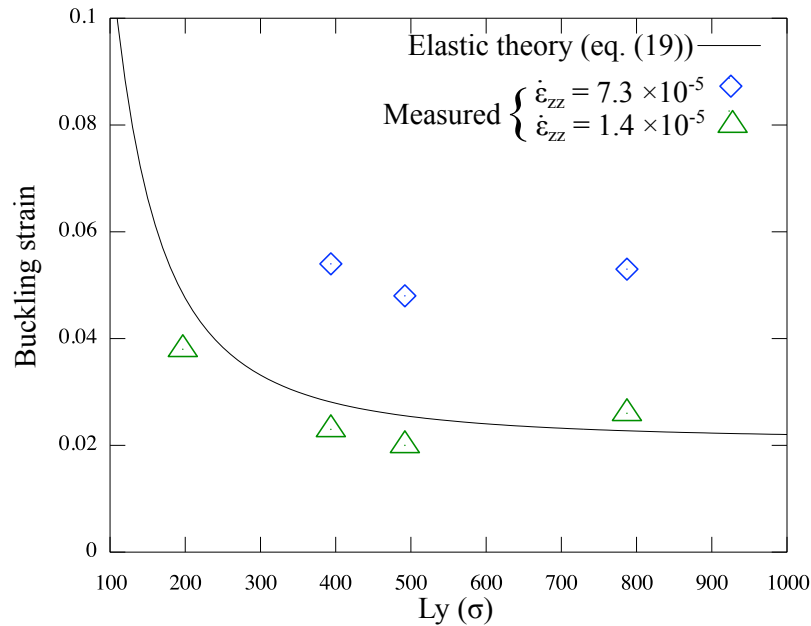


Figure 10: Comparison between the buckling strain values predicted from the elastic theory (19) and the one measured from MD simulations for all samples at two strain rates 7.3×10^{-5} and 1.4×10^{-5} .

10 compares the buckling strain values predicted from the elastic theory and the one measured from MD simulation for all samples at two strain rates. The MD buckling strain is defined by the value of the strain at which a deviation from the linear Poisson behavior is detected in the lateral strain. Elastic theory predictions (19) correspond well to MD simulation performed at low strain rate, which is not the case with high strain rate MD simulations.

Summarizing these observations, the role of the strain rate seems to be determinant for the mechanical response of the sample. Depending on the applied rate of the deformation, the samples

switch between the fundamental and the second mode of buckling or between the cavitation and buckling. In the next section, a simple model will be proposed to account for this dependence of the buckling instability on strain rate.

Unloading process

The irreversible aspect of the deformation was studied by instantaneously unloading the sample after deforming to different final strains, and monitoring the subsequent relaxation of the strain. The results of these relaxation simulations are shown in figure 11. It is seen that the process is clearly irreversible only for the largest deformation. For such deformations, significant cavitation has taken place at the hinges of the chevron pattern. The resulting density pattern under zero load displays a chevron structure with quite large angles, as observed in experiments. However, the residual, irreversible deformation is quite small, about 10% for a total deformation of 50%. This is presumably the consequence of a model in which the 'hard' phase remains in fact relatively soft (i.e. the contrast in moduli is smaller than in experiments) and irreversible damage implying chain breaking is excluded. As a consequence the main source of irreversible damage in the glassy phase is the cavitation process.

Competition between buckling modes

Modeling

The results from the previous sections show a unexpected change of wave vector with strain rate. To understand this observation, we propose to describe the growth of the buckling amplitude $U_n(t)$ for a wave-vector $k_n = 2n\pi/L_y$ using a simple linear relaxation equation of the form:

$$\frac{dU_n}{dt} = -\Lambda.F(\epsilon_{zz}, k_n).U_n \quad (20)$$

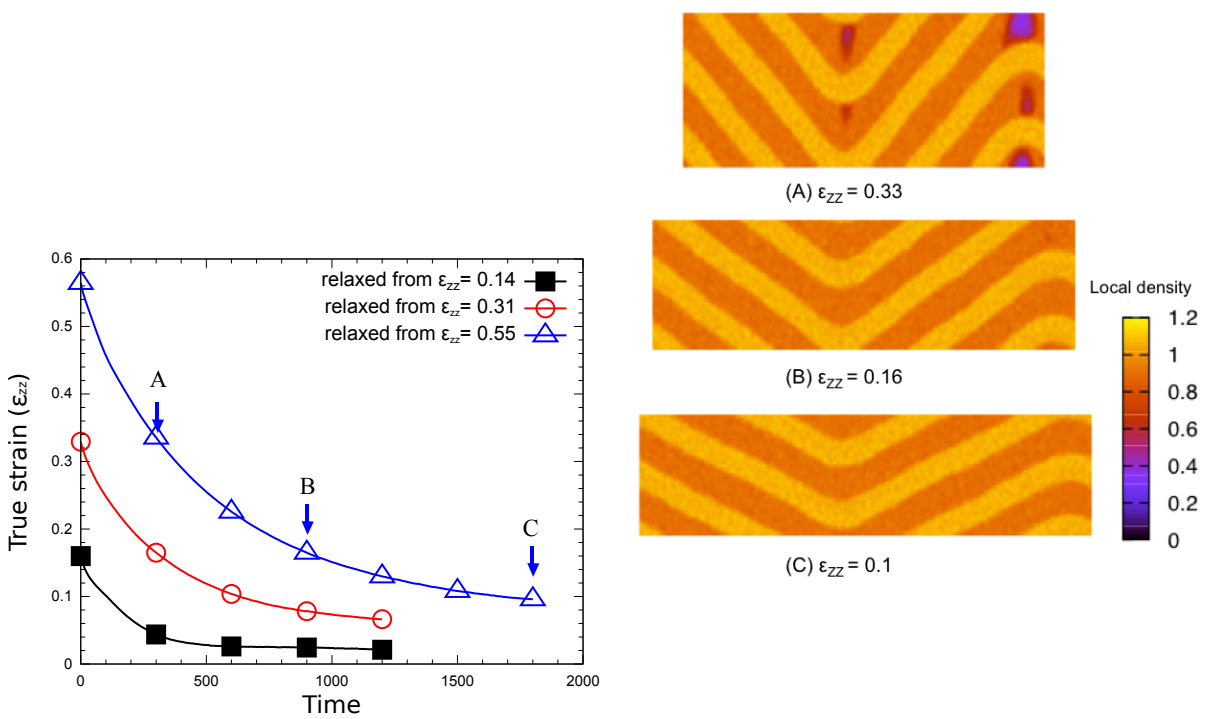


Figure 11: Left: relaxation of the strain in a system unloaded instantaneously after being deformed to the strains indicated in the figure. Right : snapshots of the relaxing configuration (density field) at the three states indicated by A,B, C in the left panel.

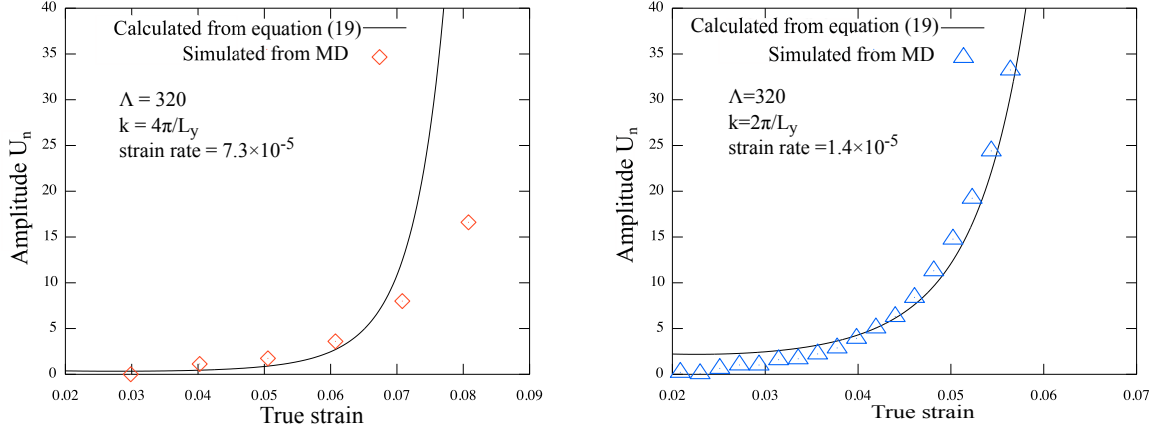


Figure 12: Comparison between the measured values of buckling amplitude (disconnected symbols) and the value calculated from equation 9 (full lines) for the largest sample $L_y = 787.2\sigma$. The left panel corresponds to fundamental mode $k = \frac{2\pi}{L_y}$ observed at low strain rate, whereas the right panel corresponds to the second mode $k = \frac{4\pi}{L_y}$ at high strain rate. The value of Λ taken here corresponds to the best fit of the measured amplitude.

where $F(\varepsilon, k_n) \cdot U_n$ is the driving force. Λ is a phenomenological coefficient which will be assumed to be independent from wave-vector and the strain rate. The solution of this equation can be written as:

$$U_n(t) = U_n(0) \cdot \exp\left(-\Lambda \cdot \int_0^t F(\varepsilon(s), k) \cdot ds\right) \quad (21)$$

Note that the strain ε_{zz} is a time dependent variable $\varepsilon_{zz}(t) = \dot{\varepsilon}_{zz} \times t$. One also remarks that $U_n(t)$ in equation 21 is not monotonous. The function passes through a minimum at short times (small strains), as the phenomenological equation 20 is purely relaxational. For large enough strains, the growth rate becomes positive, and $U_n(t)$ grows exponentially. The growth starts when ε_{zz} corresponds to the buckling strain ($\varepsilon_{zz} = \varepsilon_{zz}^*(k)$) for which $F(\varepsilon_{zz}(t), k) = 0$. The decreasing part of the curve prior to buckling is irrelevant, as thermal fluctuations are ignored in equation 20.

Equation 20 has been solved numerically using a fourth order Runge-Kutta method starting from an arbitrary small value of $U_n(0)$. The value of Λ and $U_n(0)$ were determined by the solution that ensures the best fit of the buckling amplitude measured during the deformation of the largest sample S_{24} at low and high strain rate (see figure 12). Note that the largest sample was chosen for the fit because the two buckling modes $2\pi/L_y$ and $4\pi/L_y$ can be clearly distinguished at two

different strain rates. We find that the best fit is obtained for $\Lambda = 320$ and the initial value of $U_n(0) = 0.03$. This initial value of the amplitude can be considered as corresponding to the level of heterogeneity of the initial sample, which serves to initiate the buckling.

Results and discussion

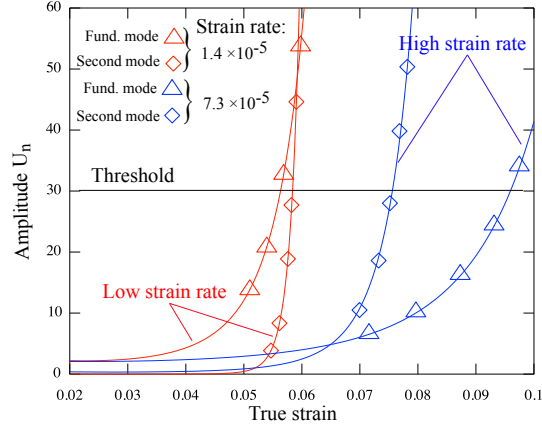


Figure 13: Comparison between the growth of the fundamental mode and of the second mode for the largest sample at two different strain rates. The higher mode develops faster than the lower mode even if the instability of the latter is triggered at first. The threshold is chosen so that it intersects first the fundamental mode at low strain rate, and the second mode at high strain rate.

Having fixed Λ and $U_n(0)$, equation 20 has been solved for different values of wave vectors $2\pi/L_y$ and $4\pi/L_y$ at two different strain rates $\dot{\epsilon}_{zz} = 7.3 \times 10^{-5}$ and $\dot{\epsilon}_{zz} = 1.4 \times 10^{-5}$. The results were plotted and compared in figure 13. This figure shows that (i) the buckling strain increases as the buckling wave vector increases, as expected; (ii) at the same strain rate, the second buckling mode is faster to develop, compared to the fundamental mode. Moreover the second mode growth intercepts the fundamental buckling growth at a certain strain (called below switching strain, ϵ_{sw}) for both strain rates. At this strain the second buckling mode can overtake the fundamental mode if the latter has not fully developed. For the low strain rate case, the fundamental buckling mode starts growing at a low strain, and is well developed when the strain reaches ϵ_{sw} , so that the system can not switch to higher buckling mode, and the fundamental mode is selected. In contrast, at high strain rate the first mode has grown to a small amplitude when the sample reaches ϵ_{sw} , so that the

second mode can easily overwhelm the fundamental mode and the sample adopts a higher mode for buckling.

From the previous analysis one can define a critical buckling amplitude: as the amplitude threshold after which the selection of the buckling mode is prohibited. This means that the buckling mode that reaches this threshold at the first is the one that is adopted by the sample to achieve the buckling. This mode is called hereafter the “winner mode”. Quantitatively speaking the “winner mode” of buckling is defined when the strain elapsed to reach the critical amplitude is minimum.

The critical amplitude threshold can be determined approximatively from figure 13. This threshold graphically located in the middle of the interval delimited by the two switching points² for each strain rate curves. For the rest of analysis the amplitude threshold was taken $U^* = 30\sigma$, at this value the threshold crosses the fundamental mode growth at first at low deformation rate while it crosses the second mode at first at high deformation rate.

Obviously, the procedure that consists in fixing the amplitude threshold at which a mode will become predominant is empirical. The actual mechanism for mode selection presumably involves nonlinear interactions between modes, which are not accounted for in the present description.

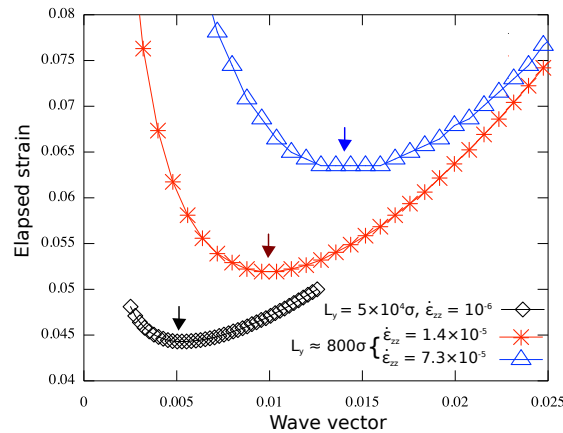


Figure 14: True strain elapsed from the beginning of the deformation to reach the threshold for different buckling wave vectors, according to the kinetic model : the minimum corresponds to the “winner mode”, that will be adopted by the sample. Several different system sizes and strain rates varying over two orders of magnitude are considered.

²This term designates the switching from the fundamental to the second mode only

Generalization

In order to generalize the previous analysis: let one consider a large sample that is deformed at an imposed strain rate $\dot{\epsilon}_{zz}$. The choice of a large sample size leads to very close values of wave vectors $2\pi/L_y \simeq 4\pi/L_y \simeq 6\pi/L_y \dots$. To identify the mode that is likely to be selected, one has to compute the growth of the amplitude for each mode, which was done using the same parameter Λ as above. The strain needed for the amplitude of a mode to reach the threshold U^* can then be computed as a function of k . The result is plotted in figure 14. The curve passes through a minimum that separates two regimes: the decreasing portion of the curve that corresponds to the fact that the development of buckling becomes faster as the buckling wave vector increases. The second regime, after the minimum, corresponds to the increase of the buckling strain observed when the buckling wave vector increases. The value of the minimum gives the wavevector that will be selected at the strain rate under consideration. Besides the approximation of using a wavevector independent threshold, this prediction also ignores the nucleation of cavities observed at extremely high strain rate, and neglects any variation of Λ with respect to the deformation rate.

Conclusion

In this paper, the mechanical response of triblock copolymer models in the lamellar phase has been investigated by using a coarse grained molecular dynamic simulation. Our MD samples were built by radical like polymerization method, and alternate glassy and rubbery lamellae. Uniaxial tensile tests were performed in the direction normal to the layers. The resulting constitutive laws are compared to the change of sample morphology and microstructure.

Depending on the applied deformation rate, the samples exhibit a variety of microscopic deformation mechanisms. At relatively high strain rate, one observes (except for the shortest samples) a buckling of the lamellae into a wavelength that does not depend on the sample size. The buckling is accompanied by the nucleation of cavities in the rubbery phase. Both events were found to contribute to the drop stress at yield. At low strain rate, all samples (including the shortest one)

exhibit buckling. The yield becomes correlated with the onset of the lamellae buckling, and the cavitation is delayed. The undulation wavelength is almost equal to the sample length in this case. The buckling strain of each sample was calculated using the elastic theory approach. The results were compared to the values observed in the MD simulations. A strong deviation was found at high strain rate; however, at low strain rate, the results are consistent.

This behavior was rationalized by using a simplified model of mode growth based on a viscous dynamics and on an elastic driving force for the mode amplitudes. This model shows that the higher mode of buckling is faster to develop compared to the fundamental mode, although the latter is the first to become unstable. When the strain rate increases, several modes come into competition. The shortest wavelength that corresponds to a larger driving force can take over and dominate the instability pattern. In this case the strain for observing buckling can be markedly larger than predicted by elastic theory.

We finally turn to a short discussion of the relevance of our results to experimental situations. Our simulations use a coarse grained model, which is not specific to any material, and is defined in terms of typical energy, mass and size. Using an energy scale of $1000K \times k_B$ and a length scale of 0.5 nm, which are typical in the coarse-grained descriptions of standard polymers, the corresponding stress unit is of order 100 MPa, and the Young modulus of the glassy polymer is of the order of 1-10 GPa. The timescale that results from these choices of units, if parameters appropriate for typical polymers are used, lies in the picosecond time range. Therefore, the strain rates achieved in simulations are of the order of $10^7 s^{-1}$ in real units, extremely high compared to typical experimental rates. As is often the case in simulation studies involving glassy materials, the behavior observed in simulation studies must be understood as being qualitatively, rather than quantitatively, representative of the experimental reality. However, there are several arguments that are indicative of the relevance of the mechanism observed and modeled in this paper to experimental situations. First of all, it is known from experiments that plasticity is usually observed for strains of at least 5%. For such values of the strain, the wavelength that are energetically favorable within the elastic theory are quite small, as can be seen from figure 5, and typically in the 100 nm range. The issue is

then to understand, why such wavelengths are selected within the experimentally slow deformation process, as opposed to larger wavelengths that should be selected in a truly quasistatic approach. Our molecular simulations and the associated kinetic model are a good indicator here. Molecular simulations indicate that the critical strain predicted by the static elastic theory is observed for the lowest strain rates that can be achieved in simulation, which are still very high compared to experiments. These results are rationalized on the basis of a kinetic model, and the extrapolation to lower strain rates using the kinetic model indicates that the preferred wavelength will be weakly sensitive to strain rate over a broad range of values, with a selected wavelength that increases by only a factor of 2 for a change of more than one order of magnitude in the strain rate (see figure 14). Unfortunately the limitations of the model, which considers a strain rate independent kinetic coefficient, does not allow us to extrapolate reliably to experimental strain rates. Another qualitative prediction that can be made on the basis of our analysis concerns the temperature dependence of the chevron pattern; as the kinetic coefficient Λ is expected to increase with temperature ($1/\Lambda$ can be associated with a viscosity), the threshold for instability will be reached earlier for larger wavelength. Therefore the wavelength is expected to increase with increasing temperature as it does with decreasing strain rate, in line with general time-temperature considerations.

Acknowledgement

Computational support was provided by the Federation Lyonnaise de Calcul Haute Performance and GENCI/CINES . Financial support from ANR project Nanomeca is acknowledged. JLB is supported by Institut Universitaire de France. Part of the simulations were carried out using the LAMMPS molecular dynamics software (<http://lammps.sandia.gov>), The snapshots were visualized using VMD software²⁴ (<http://www.ks.uiuc.edu/Research/vmd/>) .

References

- (1) Bates, F.; Fredrickson, G. *Phys. Today* **1999**, 52, 32.

- (2) Michler, G.; Adhikari, R.; Henning, S. *Journal of Materials Science* **2004**, *39*, 3281–3292.
- (3) Krumova, M.; Henning, S.; Michler, G. H. *Philosophical Magazine* **2006**, *86*, 1689–1712.
- (4) Koo, M.; Wu, L.; Lim, L.; Mahanthappa, M.; Hillmyer, M.; Bates, F. *Macromolecules* **2005**, *38*, 6090–6098.
- (5) Hermel, T.; Hahn, S.; Chaffin, K.; Gerberich, W.; Bates, F. *Macromolecules* **2003**, *36*, 2190–2193.
- (6) Burnay, S.; Groves, G. *Journal of Materials Science* **1977**, *12*, 1139–1142.
- (7) Bochl, G.; Owen, A. *Colloid and Polymer Science* **1984**, *262*, 793–797.
- (8) Bartczak, Z.; Lezak, E. *Polymer* **2005**, *46*, 6050 – 6063.
- (9) Mohanraj, J.; Morawiec, J.; Pawlak, A.; Barton, D.; Galeski, A.; Ward, I. *Polymer* **2008**, *49*, 303 – 316.
- (10) Cohen, Y.; Albalak, R.; Dair, B. *Macromolecules* **2000**, *33*, 6502.
- (11) Mori, Y.; Lim, L.; Bates, F. *Macromolecules* **2003**, *36*, 9879–9888.
- (12) Mahanthappa, M.; Hillmyer, M.; Bates, F. *Macromolecules* **2008**, *41*, 1341–1351.
- (13) Phatak, A.; Lim, L.; Reaves, C.; Bates, F. *Macromolecules* **2006**, *39*, 6221–6228.
- (14) Honeker, T., Christian C.; L., E. *Chemistry of Materials* **1996**, *8*, 1702–1714.
- (15) Diamant J., W. M. C.; S., S. D. *Polym Eng Sci* **1988**, *28*, 207–220.
- (16) Adhikari, R.; Michler, G. *Progress in Polymer Science* **2004**, *29*, 949–986.
- (17) Cohen, Y. *Macromolecules* **2001**, *33*, 6502–6516.
- (18) Read, D. J.; Duckett, R.; Sweeny, J.; McLeish, T. *J. Phys. D: Appl. phys.* **1999**, 2087–2099.

- (19) Makke, A.; Lame, O.; Perez, M.; Barrat, J.-L. *Macromolecules* **2012**, *45*, 8445–8452.
- (20) Makke, A.; Perez, M.; Lame, O.; Barrat, J. *J. Chem. Phys.* **2009**, *131*, –.
- (21) Makke, A.; Perez, M.; Lame, O.; Barrat, J. *PNAS* **2011**,
- (22) Kremer, K.; Grest, G. *The Journal of Chemical Physics* **1990**, *92*, 5057–5086.
- (23) Perez, M.; Lame, O.; Leonforte, F.; Barrat, J. *The Journal of Chemical Physics* **2008**, *128*, 234904.
- (24) Humphrey, W.; Dalke, A.; Schulten, K. *Journal of Molecular Graphics* **1996**, *14*, 33–38.

Graphical TOC Entry

